A Wearable Haptic Device for the Hand with Interchangeable End-Effectors

Lisheng Kuang, Marco Ferro, Monica Malvezzi, Domenico Prattichizzo, Paolo Robuffo Giordano, Francesco Chinello, Claudio Pacchierotti

A Wearable Haptic Device for the Hand with Interchangeable End-Effectors

Lisheng Kuang, Marco Ferro, Monica Malvezzi, Domenico Prattichizzo,
Paolo Robuffo Giordano, Francesco Chinello, Claudio Pacchierotti

***Abstract*—This paper presents a 4-degrees-of-freedom (4-DoF) hand wearable haptic device for Virtual Reality (VR). It is designed to support different end-effectors, that can be easily exchanged so as to provide a wide range of haptic sensations. The device is composed of a static upper body, secured to the back of the hand, and the (changeable) end-effector, placed in contact with the palm. The two parts of the device are connected by two articulated arms, actuated by four servo motors housed on the upper body and along the arms. The paper summarizes the design and kinematics of the wearable haptic device and presents a position control scheme able to actuate a broad range of end-effectors. As a proof of concept, we present and evaluate three representative end-effectors during interactions in VR, rendering the sensation of interacting (E1) with rigid slanted surfaces and sharp edges having different orientations, (E2) with curved surfaces having different curvatures, and (E3) with soft surfaces having different stiffness characteristics. A few additional end-effector designs are discussed. A human-subjects evaluation in immersive VR shows the broad applicability of the device, able to render rich interactions with a diverse set of virtual objects.**

***Index Terms*—Wearable haptics, Virtual Reality, Human-computer interaction**

I. Introduction

RECENT advancements in mechatronics, robotics, and smart materials have fostered the development of wearable haptic interfaces, which are considered promising tools for enhancing a broad range of human-machine and human-human interactions as well as recreate artificial touch sensations in Virtual and Mixed Reality (VR/MR) scenarios [1]. Wearable haptic devices have been developed for rendering diverse sensations across the body, providing kinesthetic [2]–[5], pressure [4], [6]–[12], skin stretch [9], [11], [13]–[16], softness [16]–[18], and/or vibratory [4], [7], [19] haptic sensations to the fingers [6], [7], [13], [14], [17]–[19], palm [8]–[12], [16], hand [2]–[4], and arm [15], [20].

Regardless the specific features and areas of applications, each haptic device can usually only convey a (very small) subset of these sensations, severely limiting the range of interactions they can render. Indeed, as providing different types of haptic cues usually means bulkier interfaces, it is rare to find wearable haptic devices capable of providing a wide set of haptic stimuli [1]. This limitation is particularly daunting in VR and MR, where the design choices for the virtual environment should not be limited by the reduced rendering capabilities of the haptic device in use. Despite this limitation, wearable haptic interfaces have been successfully and largely employed in this domain [7], [9], [13], [14], [21], [22], proving the great benefit and added value that this type of haptic interfaces can bring.

This paper presents a wearable haptic device for the palm, shown in Fig. 1. It features a 4-degrees-of-freedom (4-DoF) mechanism controlling the motion of two articulated legs that, in turn, actuate the end-effector. The device is designed to support a broad range of end-effectors that can be easily customized and exchanged for each considered scenario, so as to best render the target sensations. The design of the proposed

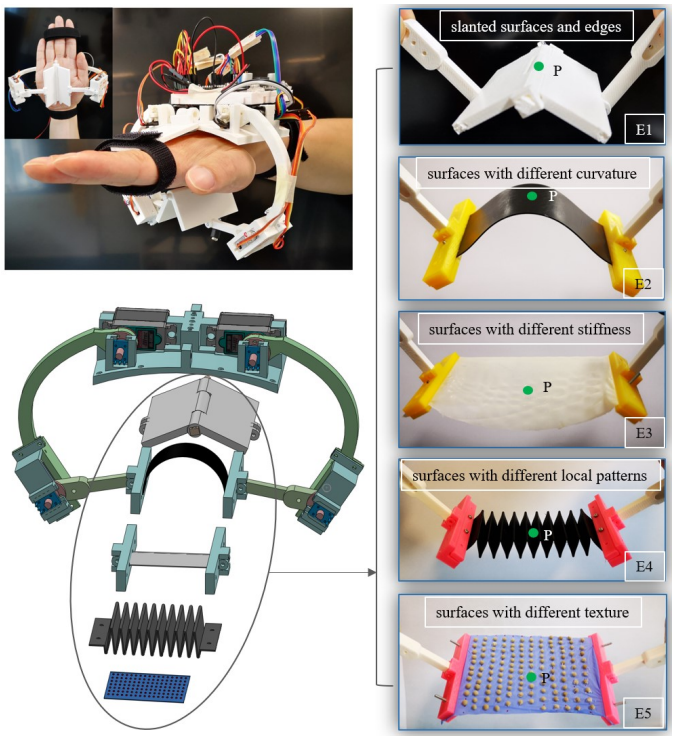

Fig. 1. The proposed 4-DoF wearable haptic device for the palm. The static upper body is fixed to the back of the hand, housing two motors. Two articulated legs, housing two additional motors, connect the upper body with the end-effector, that can be changed according to the target interaction. Here we present five end-effectors, able to simulate the sensations of interacting with: (E1) rigid slanted surfaces and sharp edges having different orientations, (E2) U-shaped soft surfaces having different curvatures, and soft surfaces having different (E3) stiffness, (E4) local shape, or (E5) texture. The first three of these end-effectors are tested in a human subjects study in VR. Of course, more end-effectors can be easily designed according to the target environment to render.

L. Kuang, M. Ferro, P. Robuffo Giordano and C. Pacchierotti are with CNRS, Univ Rennes, Inria, IRISA (Rennes, France). E-mail: {lisheng.kuang, marco.ferro, prg, claudio.pacchierotti}@irisa.fr

M. Malvezzi and D. Prattichizzo are with the Dept. Information Eng. and Mathematics, University of Siena (Siena, Italy) and with the Italian Institute of Technology (Genova, Italy). E-mail: {monica.malvezzi, domenico.prattichizzo}@unisi.it

F. Chinello is with the Dept. Business Development and Technology, Aarhus University (Herning, Denmark). E-mail: chinello@btech.au.dk

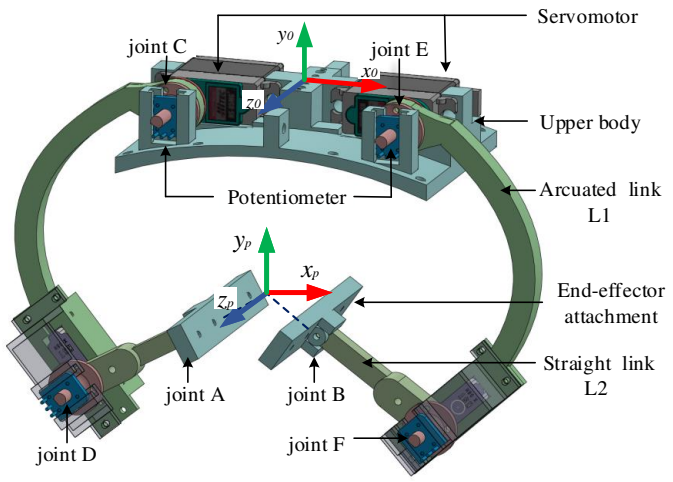

Fig. 2. CAD scheme of the proposed wearable device. It is composed of a static upper body, located on the back of the hand, and an interchangeable end-effector, placed in contact with the palm. Two articulated arms, composed of arcuated (L1) and straight (L2) sections, connect the two parts. Four servo motors, two on the upper body and two on the arms, actuate the end-effector.

device allows to easily change its end-effector without doffing the device. Moreover, we present a general kinematic analysis of the device mechanism, that can be used to evaluate the direct and inverse kinematics functions for a wide range of diverse end-effectors, well beyond those addressed in this paper. Here, as a representative example, we describe five end-effectors, which are capable of providing the sensations of breaking/making contact with rigid and soft surfaces, interacting with objects having different stiffness, curvature, local shape, texture as well as variable edges or slanted surfaces. Nonetheless, the device structure and control support the use of many other types of end-effectors, not limited to those presented here. Three of these end-effectors are quantitatively evaluated in a human-subjects experiment in immersive VR, proving the viability and flexibility of the proposed system in rendering a wide range of different sensations. A video of the device in action can be found as supplemental material and at https://youtu.be/1rs0s9UN2fI.

With respect to other wearable haptic solutions for the palm [8]–[12], [16], the proposed device can convey a significantly broader and more customizable range of stimuli. Indeed, it is rare to see reconfigurable haptic interfaces. One of the few examples is the Haptic Revolver [23], which is a handheld VR controller actuating an interchangeable wheel that raises and lowers underneath the user's finger to render contact with different textures. More recently, we presented a 3-DoF parallel tendon-based palm device able to actuate a set of rigid tactors that can have different shapes [12]. To the best of our knowledge, no wearable reconfigurable haptic solution for the palm have been presented in the literature. A preliminary version of our device, featuring a rigid non-changeable end-effector, has been presented in [24]. Here we improve the device design and control to support interchangeable end-effectors, discuss the rendering characteristics of five end-effectors, and present a human-subjects evaluation on three of them in VR.

TABLE I
DEVICE SPECIFICATIONS

Weight	160 g
Dimension Length × Width × Height	(13–18) × 18 × (12–15) cm
Maximum contact surface	42 cm^2
Control system	Arduino Uno, Atmega328
Operating voltage range	4.8 to 6.0 V
Operating joints speed	0.14 sec/60°
Maximum horizontal displacement	9 cm
Maximum vertical displacement	5 cm

II. WEARABLE DEVICE AND INTERCHANGEABLE END-EFFECTORS

The general design of the wearable haptic device, together with its mobility, statics, and manipulability, as well as direct, inverse, and differential kinematics is presented in [24]. Here we summarize the main aspects, focusing on the improvements made to enable the support of interchangeable end-effectors. We also describe the three representative end-effectors that we have chosen to display the features of the device.

The prototype of the wearable device is shown in Fig. 1 while its CAD design in presented in Fig. 2. The device features a 4-DoF structure with two symmetric serial arms connecting the chosen end-effector to the static upper body, which is in turn fastened to the back of the hand with velcro straps. Each arm consists of an arcuated link (L1 in Fig. 2) and a straight link (L2), forming a rigid serial chain constrained to each other. The arcuated links of each arm connect to the upper body with joints C and E, as well as to the corresponding straight links L2 through two lower revolute joint D and F. Joints C, E, D, and F are actuated by servomotors. The axes of the revolute joints are parallel to each other, making the whole mechanism planar. Finally, each straight link L2 is connected to the chosen end-effector through a passive revolute joint, generating a 2-DoF planar articulated mechanism. The combined action of the two arms leads to the final 4 DoF of the system, making the two end points of the legs, A and B, move vertically and horizontally across the plane defined by axes x_0–y_0 in Fig. 2.

Given the above kinematics constraints, it is possible to design end-effectors that cover a wide range of interactions, according to the task at hand. The end-effectors can be attached to the straight links of the device, between the joints indicated with A and B in Fig. 2.

In our prototype, we controlled the device using an Atmega328 controller on an Arduino Uno Board. We used two HS-85MG (Hitech RCD, US) servomotors on the upper body, actuating joints C, E, and two KST-08H (KST servos, HK) servomotors on the arms, actuating joints D, F. Rotatory Bourns potentiometers 3382H (Bourns, CA, US) are installed in each servomotor shaft, so as to measure the motor's rotation angle. Fig. 3 shows a series of representative motions that the device can actuate, while Table I summarizes its main characteristics.

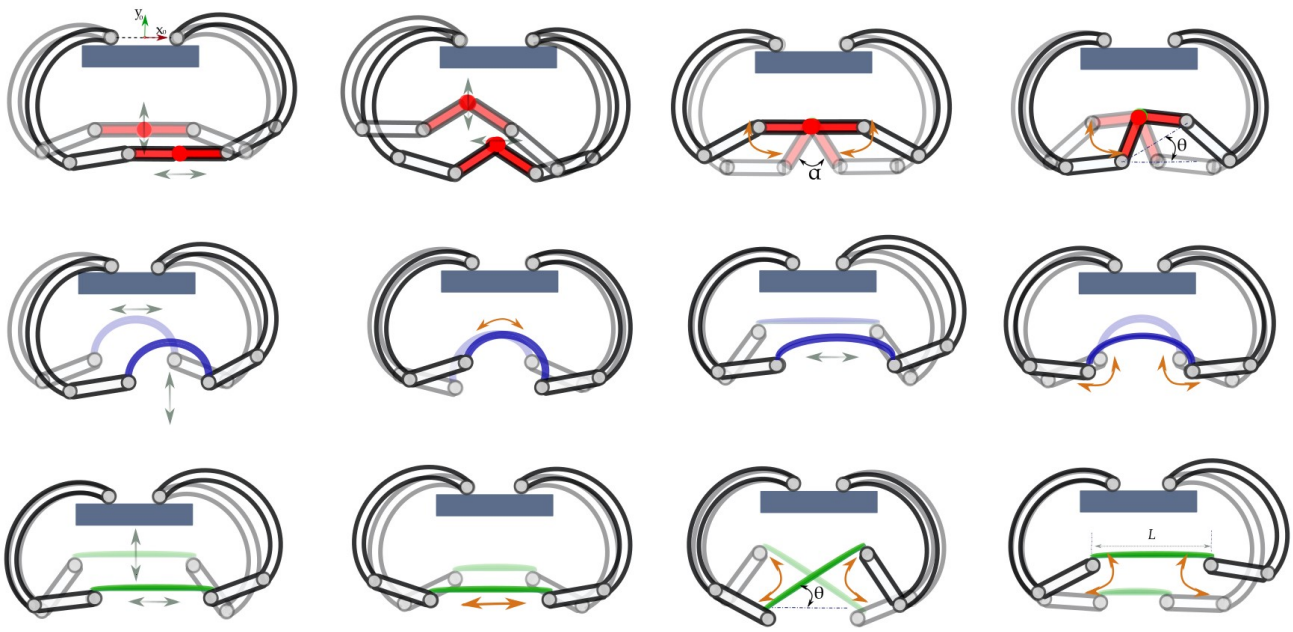

Fig. 3. Representative movements of the wearable device when equipped with end-effectors E1 (top, in red), E2 (middle, in blue), and E3 (bottom, in green). The end-effectors, in green, are actuated by the joint action of the arcuated and straight links, rolling and moving horizontally/vertically on a plane. In addition to these motions, E1 can fold and unfold, simulating the interaction with rigid slated surfaces and edges; E2 can adjust the local curvature, simulating the interaction with soft slanted surfaces having different curvatures; and E3 can stretch, simulating the interaction with soft slanted surfaces having different stiffness characteristics.

A. *Five representative end-effectors*

As a proof of concept, we designed five end-effectors (E1–E5), able to render different sets of sensations. The first three end-effectors are then evaluated in the human subjects experiment of Sec. IV.

E1. Rigid hinge-like end-effector, shown in Fig. 1-E1: It is composed of two flat rectangular plates connected in a hinge-like fashion through a passive revolute joint, allowing the folding of the two plates around the z_0 direction (see Fig. 2). Actuated by the combined action of the two arms, the movement of the end-effector is constrained within the x_0–y_0 plane, constituted by the joints. In this way, the end-effector can be controlled to move vertically along the y_0 axis, sideways along the x_0 axis, fold, and roll. However, since the three joints on the end-effector are passive, we cannot control the direction of the folding, i.e., we cannot control whether the edge created by the folding points upwards or downwards. We included a stopper on the revolute joint between the two plates to constraint the end-effector to fold with the edge pointing upwards, so as to generate the sensation of interacting with edges of different sharpness. Of course, the stopper can be easily adjusted to constraint the end-effector to fold in the other direction. This end-effector can provide the sensation of interacting with rigid slanted surfaces and edges. A video showing the motion of this end-effector is reported in https://youtu.be/1rs0s9UN2fIs?t=23. A preliminary version of this end-effector was used in [24], where its kinematic model is described in detail, and later also in [25].

E2. Soft U-shaped end-effector, Fig. 1-E2: It is composed of a flexible rectangular strip of PolyFlex TPU90 (thermoplastic polyurethane), having dimensions 40×110×1.2 mm (width×length×thickness). As for all end-effectors, its short ends are rigidly clamped to the distal parts of the device's straight links L2 (A and B in Fig. 2). Actuated by the combined action of the two arms, the movement of the end-effector is again constrained within the x_0–y_0 plane, creating reversed U-shapes with different curvatures as the two arms move closer/farther from each other (see Sec. III-A for its model). The clamping structure forces the end-effector to bend in the upper direction, similarly to how the rigid hinge-like end-effector E1 folds. This second end-effector can render 4 DoF movements vertically along the y_0 axis, sideways along the x_0 axis, as well as roll, and bend in a reversed U shape, providing the sensation of interacting with soft shapes having different curvatures and orientations. A video showing the motion of this end-effector is reported in https://youtu.be/1rs0s9UN2fIs?t=33. Changing the thickness of the TPU strip, we can adjust the stiffness of the end-effector to the target task and environment.

E3. Elastic rubber end-effector, Fig. 1-E3: It is composed of a flexible rectangular strip of latex rubber, having dimensions 40×110×0.1 mm (width×length×thickness). This material has a 4.69 Mpa Young Modules and 18.36 Mpa tensile strength, making it rather flexible yet very resistant. Actuated by the combined action of the two arms, the end-effector can stretch and roll, creating the sensation of interacting with soft surfaces having different stiffness and orientation. The more it is stretched, the stiffer it is (see Sec. A for its characterization). A video showing the motion of this end-effector is reported in https://youtu.be/1rs0s9UN2fIs?t=41.

E4. Triangular origami end-effector, Fig. 1-E4: It is composed of a flexible rectangular origami structure made of PolyFlex TPU90, having dimensions 40×70×0.8 mm

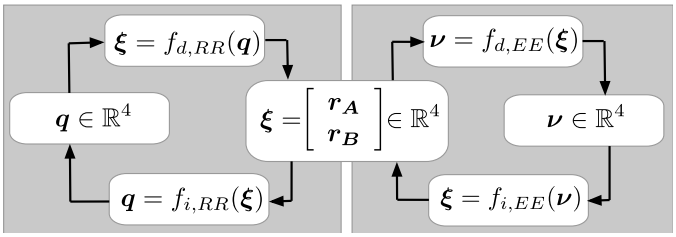

Fig. 4. Kinematic analysis scheme. We can identify two main parts. The first one relates joint rotation angles $\mathbf{q}$ with A and B point positions, collected in the vector $\boldsymbol{\xi}$, and it is independent from the end-effector. The second one relates A and B point positions to the output vector $\boldsymbol{\nu}$, and it depends on the specific end-effector characteristics.

(width×lengthspan×thickness). The structure folds in a series of triangular shapes whose edges get farther to each other as the end-effector is stretched out. Actuated by the combined action of the two arms, the end-effector can stretch and roll, creating the sensation of interacting with surfaces having different local patterns, i.e., variable spaced ridges in this case, and orientation.

E5. Texture elastic end-effector, Fig. 1-E5: It is composed of a flexible rectangular strip of Nitrile rubber, having dimensions 40×110×0.1 mm (width×length×thickness). This material has a 2.10 Mpa Young Modules and 22 Mpa tensile strength. Small plastic grains of 1 mm diameter are homogeneously glued to the surface so as to render the sensation of interacting with a rough surface. As the elastic end-effector is stretched, the grains become more distant from each other, lowering their local density and, in turn, the perceived roughness of the surface. Actuated by the combined action of the two arms, the end-effector can stretch and roll, creating the sensation of interacting with soft surfaces having different texture and orientation.

III. Device Kinematic Analysis

This Section describes the mechanical model of the device, including its mobility analysis as well as the forward and inverse kinematics analysis, necessary to derive the main structural parameters of the device and for the definition of position control algorithms. As shown in Figs. 2 and 5, the revolute joints are parallel to each other and perpendicular to the reference plane Σ, defined by x_0 and y_0. Let us indicate with C, D, E, and F the intersection points between the revolute joint axes and the Σ plane. Let us indicate with $S_0 < O_0, x_0, y_0, z_0 >$ the reference frame attached to the upper body, in which O_0 is the origin located in the midpoint between C and E points. The x_0 axis is parallel to $\overrightarrow{CE}$, y_0 is in the same plane with x_0, C, and E (plane Σ), and z_0 is consequently defined (see also Fig. 2). The two arcuated links L1 have the same structure, their configuration is defined by vectors $\overrightarrow{CD}$ and $\overrightarrow{EF}$, respectively, with length $|\overrightarrow{CD}| = |\overrightarrow{EF}| = l_1$. The straight links L2, connecting the arcuated links to the end-effector, are defined by the vectors $\overrightarrow{DA}$ and $\overrightarrow{FB}$, respectively, with length $|\overrightarrow{DA}| = |\overrightarrow{FB}| = l_2$.

The device can be represented by two symmetrical serial planar Revolute-Revolute (R-R) chains sharing the same base, represented by the upper body, and the interchangeable rigid/deformable end-effector, constraining their movement and defining a closed-loop planar mechanism.

The analysis of the mechanism can be divided in two main parts, as summarized in Fig. 4. The first part is independent from the end-effector in use, relating joint rotation angles $\mathbf{q}$ with A and B point positions. The second part depends on the characteristics of the end-effector, relating A and B point positions to the end-effector output vector $\boldsymbol{\nu}$. For this reason, we introduce an intermediate set of variables, defining the state between the serial R-R mechanisms and the end-effector. Let us indicate with $\mathbf{q} = [q_1, q_2, q_3, q_4]^{\mathrm{T}} \in \mathbb{R}^4$ the vector containing the input variables, corresponding to the actuators' rotation angles of joints in C, D, E, and F, respectively. Let us also indicate with $\boldsymbol{\nu}$ the vector containing the output variables, whose definition depends on the specific end-effector, and with $\boldsymbol{\xi} = [x_A, y_A, x_B, y_B]^{\mathrm{T}} \in \mathbb{R}^4$ the intermediate state defining the position of A and B points, respectively. While $\mathbf{q}$ and $\boldsymbol{\xi}$ are the same regardless the end-effector in use, $\boldsymbol{\nu}$ depends on the end-effector employed. Specifically, for the end-effectors considered in this paper, the following output vectors can be defined for E1, ..., E5:

$$\boldsymbol{\nu}_{E1} = [x_P, y_P, \theta, \alpha]^{\mathrm{T}}, \tag{1}$$

where x_P, y_P are the coordinates of the middle point of the revolute joint in the end-effector edge (see Fig. 1-E1 and [24]), θ is the tilt angle (i.e., the angle between $\overline{AB}$ and x_0, see Fig. 3-top), and α is the folding angle of the end-effector (see again Fig. 3-top);

$$\boldsymbol{\nu}_{E2} = [x_P, y_P, \theta, R]^{\mathrm{T}}, \tag{2}$$

where x_P, y_P are the coordinates of the midpoint of the AB arc (see Figs. 1-E2 and 5b), θ is again the tilt angle (see Fig. 5b), and R is the curvature radius of the end-effector at P;

$$\boldsymbol{\nu}_{E3} = \boldsymbol{\nu}_{E4} = \boldsymbol{\nu}_{E5} = [x_P, y_P, \theta, L]^{\mathrm{T}}, \tag{3}$$

where x_P, y_P are the coordinates of the midpoint of the AB segment (see Figs. 1-E3, 1-E4, 1-E5), θ is again the tilt angle (see Fig. 3-bottom), and L is the distance between A and B (see again Fig. 3-bottom).

Direct kinematics analysis aims at defining the relationship mapping $\mathbf{q}$ into $\boldsymbol{\nu}$, i.e.,

$$\boldsymbol{\nu} = f_d(\mathbf{q}). \tag{4}$$

while inverse kinematics analysis defines the relationship mapping $\boldsymbol{\nu}$ into $\mathbf{q}$, i.e.,

$$\mathbf{q} = f_i(\boldsymbol{\nu}), \tag{5}$$

By introducing the intermediate state $\boldsymbol{\xi}$ these functions can be further expressed as

$$\boldsymbol{\nu} = f_{d,EE}(\boldsymbol{\xi}) = f_{d,EE}(f_{d,RR}(\mathbf{q})), \tag{6}$$

and

$$\mathbf{q} = f_{i,RR}(\boldsymbol{\xi}) = f_{i,RR}(f_{i,EE}(\boldsymbol{\nu})), \tag{7}$$

where $f_{d,RR}$ and $f_{i,RR}$ represent the direct and inverse kinematics functions for the two planar R-R mechanisms, that are the same for all the configurations, while $f_{d,EE}$ and $f_{i,EE}$

are the direct and inverse kinematics functions specific to the end-effectors.

A. From joint variables $\mathbf{q}$ to A and B position and vice-versa

Given the input variables $\mathbf{q}$, the coordinates $A = (x_A, y_A)$ and $B = (x_B, y_B)$ can be evaluated as in standard planar R-R robots, i.e.,

$$x_A = x_C + l_1 \cos(q_1) + l_2 \cos(q_1 + q_2) \quad (8)$$
$$y_A = y_C + l_1 \sin(q_1) + l_2 \sin(q_1 + q_2) \quad (9)$$
$$x_B = x_E + l_1 \cos(q_3) + l_2 \cos(q_3 + q_4) \quad (10)$$
$$y_B = y_E + l_1 \sin(q_3) + l_2 \sin(q_3 + q_4) \quad (11)$$

Eqs. (8), ..., (11) define the direct kinematic function $f_{d,RR}$. On the other hand, to define $f_{i,RR}$, we need to find $\mathbf{q}$ vector when A and B point positions are known. The problem consists in solving the inverse kinematics of two standard 2-DoF R-R planar manipulators. For the sake of brevity, the procedure is not reported here but the reader can refer to, e.g., [26].

B. Direct and inverse kinematics for the end-effectors

This Section reports the direct and inverse kinematics functions for the three end-effectors E1, E2, and E3 considered in our evaluation. A similar reasoning can be used to evaluate the direct and inverse kinematics functions for other end-effectors, enlarging the type of renderable sensations through this device.

E1. Rigid hinge-like end-effector: In the direct kinematic problem from A and B coordinates, it is possible to evaluate angle θ as

$$\theta = \arctan\left(\frac{y_B - y_A}{x_B - x_A}\right), \quad (12)$$

and the distance between A and B as

$$L = \sqrt{(x_B - x_A)^2 + (y_B - y_A)^2}. \quad (13)$$

Since the considered device has a parallel structure, the input variables $\mathbf{q}$ are constrained by the structure. In particular, length L has to satisfy the following inequality:

$$L \leq 2l_3. \quad (14)$$

If this constraint is satisfied, the folding edge angle α ans P coordinates can be evaluated, as detailed in [24].

In the inverse kinematic problem for this end-effector, vector $\boldsymbol{\xi}$ components are evaluated as a function of a set of output variables $\boldsymbol{\nu}_{E1}$, i.e.,

$$\boldsymbol{\xi} = \mathrm{f}_{\mathrm{i,EE}}(\boldsymbol{\nu}_{\mathrm{E1}}).$$

Also in this case, the procedure is detailed in [24].

E2. Soft U-shaped end-effector: As before, in the direct kinematic problem for this end-effector, given vector $\boldsymbol{\xi}$, θ angle can be evaluated by eq. (12), while L can be evaluated by eq. (13). However, for this end-effector, the congruence control reported in eq. (14) should be substituted by

$$L_m \leq L \leq L_0,$$

where L_m represents a lower limit defined according to the end-effector mechanical properties, while L_0 is the upper limit,

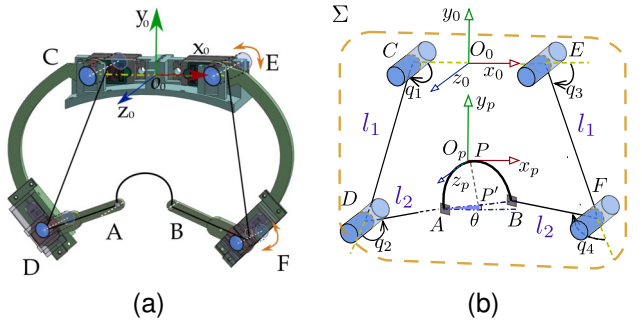

Fig. 5. Kinematic structure of the proposed device when equipped with the soft U-shaped end-effector (E2). Point P is placed at the vertex of the bent end-effector, which has fixed length and is attached to points A and B. Point P' is placed at the middle between $\overline{AB}$. Two planar Revolute-Revolute (R-R) chains, actuated by four motors, move the end-effector, providing the user with the sensation of interacting with soft objects having different curvatures.

corresponding to a flatten end-effector. In the case of our implementation of E2, $L_m = 40$ mm and $L_0 = 115$ mm. The curvature radius R, assumed constant across the end-effector, can be evaluated by solving the following nonlinear equation:

$$2R \sin\left(\frac{L_0}{2R}\right) = L.$$

Finally, the coordinates of P, representing the midpoint on the U-shape end-effector, can be calculated as

$$x_P = x_{P'} - R\left(1 - \cos\left(\frac{L_0}{2R}\right)\right)\sin(\theta)$$
$$y_P = y_{P'} + R\left(1 - \cos\left(\frac{L_0}{2R}\right)\right)\cos(\theta),$$

where P' is the midpoint of $\overline{AB}$.

In the inverse kinematic problem for this end-effector, we assume that the target curvature is known and can be approximated by a quadratic function. We then consider generic quadratic set of functions $f(x) = ax^2 + bx + c$, where b can be zero. To obtain the $\hat{f}(x)$ fitting the simulated curvature $1/R$, with R being the radius, a least square fitting method can be applied,

$$\min_{a,c} ||\mathcal{C}(x, R) - \hat{f}(x)||^2,$$

where $\mathcal{C}(x, R)$ is the curve resembling the target U shape, which depends on R. In Fig. 5b, the kinematic scheme of our device equipped with E2 is shown. When vector $\boldsymbol{\nu}_{E2} = [x_P, y_P, \theta, R]$ is known, x_B can be obtained through the Newton-Raphson method as solution of the integral equation

$$\int_0^{x_B} \sqrt{1 + (d\hat{f}(x)/dx)^2}dx = L_0/2, \quad (15)$$

where L_0 is the maximum extension possible for the flexible strip and corresponds to the maximum distance between A and B, i.e., when the end-effector E2 is flat. Finally, coordinates A and B can be obtained as

$$x_A = x_P + |\overline{PP'}|\sin(\theta) - (x_P - x_A)\cos(\theta)$$
$$y_A = y_P - |\overline{PP'}|\cos(\theta) - (x_P - x_A)\sin(\theta)$$
$$x_B = x_P + |\overline{PP'}|\sin(\theta) + (x_P - x_A)\cos(\theta)$$
$$y_B = y_P - |\overline{PP'}|\cos(\theta) + (x_P - x_A)\sin(\theta).$$

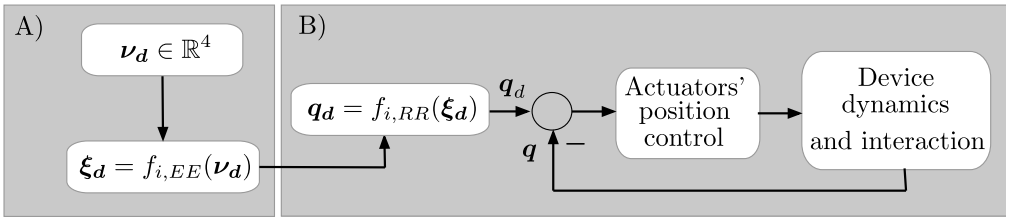

Fig. 6. Control system. According to the definitions provided in the kinematics analysis of Sec. III, the control system can be divided in two main parts. Part A) consists of the definition of the control input and depends on the specific end-effector. The task is defined in the end-effector space, providing the target output vector $\boldsymbol{\nu}_d$. Through the inverse kinematics, the intermediate vector $\boldsymbol{\xi}_d$ can be evaluated. Part B) is relative to the actuators' position control and is independent from the end-effector. Starting from $\boldsymbol{\xi}_d$, we evaluate the corresponding reference values $\mathbf{q}_d$ for actuating the joint angles. Finally, a PID position control can be employed to actuate each actuator.

E3. Elastic rubber end-effector: In the direct kinematic problem for this end-effector, recalling the definition of the output vector $\boldsymbol{\nu}_{E3}$ of eq. (3) and indicating the midpoint of $\overline{AB}$ as P, we can evaluate its coordinates as a function of $\boldsymbol{\xi}$,

$$x_P = (x_A + x_B)/2, \tag{16}$$
$$y_P = (y_A + y_B)/2. \tag{17}$$

Then, θ can be evaluated as in eq. (12), while L can be evaluated as in eq. (13). In this case, the congruence control originally introduced in eq. (14) should be substituted by

$$L_0 \leq L \leq L_M, \tag{18}$$

where L_M represents an upper limit defined on the basis of end-effector material and device structure, i.e., the maximum the end-effector can be stretched, while L_0 is a lower limit necessary to guarantee that the end-effector is taut, i.e., the minimum the end-effector should be stretched to keep it straight. Note that the L_0 parameter represents, both for E2 and E3 end effectors, the length of $\overline{AB}$ when the end-effector is straight and unstretched. This value represents the upper limit for E2 end-effector and the lower one for E3. In the case of our implementation of E3, $L_M = 170$ mm and $L_0 = 134$ mm. Finally, by controlling the stretch applied to the end-effector

$$\delta = L - L_0, \tag{19}$$

we can control its stiffness k. This relationship between the stretch and the stiffness of the material is experimentally evaluated and modelled in the Appendix. Eqs. (16), (17), (12), and (13) define the direct kinematics function $f_{d,EE}$ for end-effector E3.

In the inverse kinematic problem for this end-effector, given $\boldsymbol{\nu}_{E3}$ from eq. (3), A and B coordinates can be straightforward calculated as

$$x_A = x_P - \frac{L}{2}\cos\theta, \tag{20}$$
$$y_A = x_P - \frac{L}{2}\sin\theta, \tag{21}$$
$$x_B = x_P + \frac{L}{2}\cos\theta, \tag{22}$$
$$y_B = x_P + \frac{L}{2}\sin\theta. \tag{23}$$

Eqs. (20), ..., (23) define the inverse kinematics function $f_{i,EE}$ for the end-effector E3. This procedure can also be extended to end-effectors E4 and E5.

C. Control

The control system of the device can also be divided in two parts, similarly to the kinematics analysis. As shown on the left-hand side of Fig. 6, one part consists of the definition of the control input and depends on the specific end-effector. In this block, the task is defined in the end-effector space, providing the end-effector-dependent target output vector $\boldsymbol{\nu}_d$. Through the inverse kinematic relationships described before, the correspondent value of $\boldsymbol{\xi}_d$ vector can be evaluated. As shown on the right-hand side of Fig. 6, the second part of the control scheme is independent from the specific end-effector. From $\boldsymbol{\xi}_d$, we evaluate the corresponding reference values $\mathbf{q}_d$ for actuating the joint angles. Then, a standard PID-based position control is used to control each actuator.

IV. Experimental Evaluation

We evaluated the effectiveness of our device in rendering diverse contact interactions in immersive Virtual Reality. As a proof of concept, as mentioned before, we considered interactions with three of the five end-effectors described in Sec. II-A, i.e., E1, E2, and E3 (see also Fig. 1). For controlling each of these end-effectors, we employed the appropriate control strategy described in the Section above.

A. Participants

Twelve subjects participated in the study (10 males, 2 females, all right-handed, palm length 9.3–12.8 cm, palm breadth 8.5–11.5 cm). None of the participants reported any deficiencies in their visual or haptic perception abilities. The experimenter explained the procedures and spent about three minutes adjusting the setup to be comfortable before the subject began the experiment.

B. Experimental setup and protocol

Participants were asked to wear the proposed haptic device on their right hand, as shown in Figs. 1 and 7b. On top of the haptic device, we mounted an HTC Vive tracker, so as to track the position of the user's hand. Finally, participants were asked to wear an HTC Vive headset and sit comfortably on a chair.

The virtual environment was composed of a rotating carousel, inspired from [27] and shown in Fig. 7a, which presented the user with nine different objects to interact with.

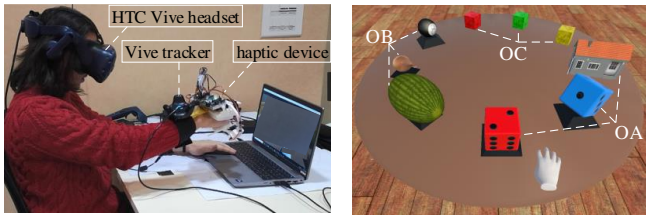

Fig. 7. (a) Experimental setup showing a user wearing the HTC Vive headset and the proposed haptic device, while interacting with the objects in the virtual environment. (b) The carousel of objects rendered in the virtual environment, divided into three main groups according to their characteristics.

TABLE II
MAIN CHARACTERISTICS OF THE VIRTUAL OBJECTS ON THE CAROUSEL

Object	Main characteristics
1 - rigid red dice	10×10×10 cm, flat surface on top
2 - rigid blue dice	10×10×10 cm, 90° edge on top
3 - rigid house rooftop	8×15×20 cm, 50° edge on top
4 - "watermelon" shape	curvature κ=3 cm^{-1}
5 - "8-ball" shape	curvature κ=5 cm^{-1}
6 - "onion" shape	curvature κ=7 cm^{-1}
7 - soft green cube	5×5×5 cm, isotropic stiffness k=26 N/mm
8 - soft yellow cube	5×5×5 cm, isotropic stiffness k=31 N/mm
9 - soft red cube	5×5×5 cm, isotropic stiffness k=36 N/mm

The objects were designed to present a wide range of diverse physical characteristics, which can rarely be rendered by a single haptic device or end-effector: three objects have rigid edges, three are curved, and three are soft. The advantages of our device is that it can support diverse end-effectors, so that it is possible to choose which one to use according to the target interaction(s). Their main characteristics are reported in Table II.

The participants interacted with each object on the carousel using the wearable device equipped with all the three considered end-effectors, leading to 3 (end-effectors) × 9 (objects) × 12 (participants) = 324 total interactions. Participants could touch each object how many times and how long they wanted. On average, they spent 10 s on each object. A button next to the carousel enabled the participant to rotate the carousel, so as to interact with a new object. For each object and for each end-effector, participants were asked to answer the question: "How realistic was the interaction with this virtual object?," yielding to 27 ratings per participant. At the end of the whole experiment, participants were also asked four additional questions: "How comfortable was the interaction with this end-effector?", "How accurate was the contact rendering with this end-effector?" and "How tired are you?". Questions were adapted from the System Usability Scale (SUS) questionnaire. Participants could answer the questions using a slider that went from 1 "not at all" to 10 "very much".

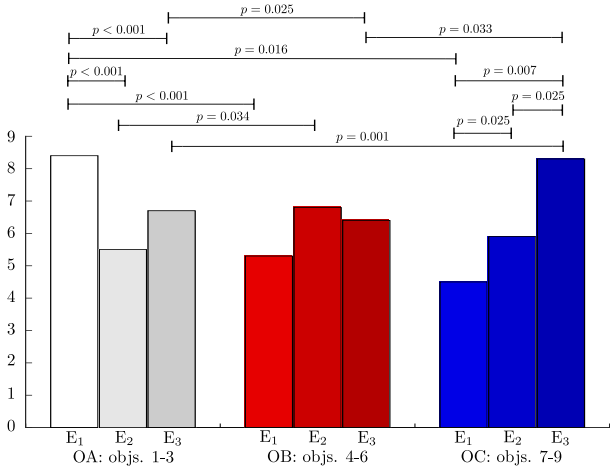

Fig. 8. Mean ratings evaluating the realism of the interaction, from the answer to "How realistic was the interaction with this virtual object?".

C. Results

Fig. 8 shows the ratings given by the participants when interacting with the three sets of objects through end-effectors E1, E2, and E3 regarding the question "How realistic was the interaction with this virtual object?". The first set gathers the three rigid objects featuring different edges and slanted surfaces (OA: objects 1–3 in Table II and Fig. 7a), the second set the three objects featuring different curvature characteristics (OB: objects 4–6), and the third set the three objects featuring different stiffness characteristics (OC: objects 7–9). To compare the ratings, we ran a two-way repeated-measures ANOVA test. The type of end-effector (E1, E2, E3) and the sets of objects (OA, OB, OC) were treated as within-subject factors. Transformed data (arcsine square root transformation) passed the Shapiro–Wilk normality test and Mauchly's Test of Sphericity. The two-way repeated-measure ANOVA revealed a statistically significant two-way interaction between the end-effector and the sets of objects variables ($F(4, 44) = 18.958, p < 0.001$). When a statistically significant interaction between variables is found, we need to analyze the simple main effects. Interpreting the simple main effects for the end-effector variable, we found a statistically significant difference (E1-OA vs. E1-OB vs. E1-OC: $F(2, 22) = 13.964, p < 0.001$, partial $\eta^2 = 0.599$; E2-OA vs. E2-OB vs. E2-OC: $F(2, 22) = 4.220, p = 0.028$, partial $\eta^2 = 0.277$; E3-OA vs. E3-OB vs. E3-OC: $F(2, 22) = 17.236, p < 0.001$, partial $\eta^2 = 0.610$). Interpreting the simple main effects for the objects variable, we found a statistically significant difference (E1-OA vs. E2-OA vs. E3-OA: $F(2, 22) = 20.421, p < 0.001$, partial $\eta^2 = 0.650$; E1-OC vs. E2-OC vs. E3-OC: $F(2, 22) = 15.419, p < 0.001$, partial $\eta^2 = 0.405$). Results of post hoc analysis with Bonferroni adjustments are reported in Table III (only significant p values are shown). The highest ratings were registered for end-effectors E1, E2, and E3 when rendering objects OA, OB, and OC, respectively.

Similarly, we ran a one-way repeated-measures ANOVA test regarding the questions "How comfortable was the interaction?" and "How accurate was the interaction?". Transformed data passed the Shapiro–Wilk normality test and Mauchly's

TABLE III
EXPERIMENTAL EVALUATION

Subjects	12 (2 females, 10 males)
Task	Interact with nine virtual objects using the considered three end-effectors.
Conditions	Type of end-effector E1 (rigid hinge-like end-eff.), E2 (soft U-shaped end-eff.), E3 (elastic rubber end-eff.) Sets of objects OA (objs. 1–3), OB (objs. 4–6), OC (objs. 7–9)

"How realistic was the interaction with this virtual object?"
Statistical analysis (only significant p values)
Simple main effect of the type of end-effector

E1-OA vs. E1-OB	$p < 0.001$	E1-OA vs. E1-OC	$p = 0.016$
E2-OA vs. E2-OB	$p = 0.034$	E3-OA vs. E3-OB	$p = 0.025$
E3-OA vs. E3-OC	$p = 0.001$	E3-OB vs. E3-OC	$p = 0.033$

Simple main effect of the sets of objects

E1-OA vs. E2-OA	$p < 0.001$	E1-OA vs. E3-OA	$p < 0.001$
E1-OC vs. E2-OC	$p = 0.025$	E1-OC vs. E3-OC	$p = 0.007$
E2-OC vs. E3-OC	$p = 0.025$		

"How comfortable was the interaction?"
Ratings were 7.7/10, 6.5/10, and 8.0/10 for end-effectors E1, E2, and E3, respectively.

"How accurate was the interaction?"
Average ratings were 7.8/10, 6.3/10, and 7.1/10 for end-effectors E1, E2, and E3, respectively.

"How tired are you?"
The average rating was 3.1/10.

Test of Sphericity. The ANOVA revealed no statistically significant difference between end-effectors for both questions. The highest ratings were registered for E3 with respect to the "comfortable" question and for E1 for the "accurate" question.

V. Discussion and Conclusion

We presented a 4-DoF hand wearable haptic device for interacting in Virtual Reality (VR). It is composed of a static upper body, secured to the back of the hand, and the (changeable) end-effector, placed in contact with the palm. The two parts of the device are connected by two articulated arms, actuated by four servo motors housed on the upper body and along the arms. The device is designed to support different end-effectors, that can be easily and quickly exchanged to provide a wide range of haptic sensations. The end-effector can be changed in less than a minute without doffing the device. Moreover, the provided kinematic analysis enables easy adaptation of the control approaches for any chosen end-effector. In this paper, we discuss the direct and inverse kinematics for three representative end-effectors; however, a similar reasoning can be used to evaluate the kinematics functions for other end-effectors, according to the interaction at hand. Doing so, this wearable device addresses one of the main limitations of wearable haptic interfaces, i.e., the limited range of sensations they can provide, in a rather inexpensive and comfortable package.

The paper presented the design and kinematics of the proposed haptic device together with a position control scheme able to actuate generic end-effectors during VR interaction. The paper also discusses, as a proof of concept, five representative end-effectors, able to render the sensation of interacting (E1) with rigid slanted surfaces and sharp edges having different orientations, (E2) with curved surfaces having different curvatures, and with soft surfaces having different (E3) stiffness characteristics, (E4) local shape, and (E5) texture. Of course, many more end-effectors can be designed, according to the type(s) of interaction at hand.

The first three of these end-effectors, E1, E2, and E3, have been evaluated in a human-subjects study in immersive VR. The 12 participants proved that the considered end-effectors are capable to render rather realistic interactions in VR. Participants also found the device comfortable to wear and use, and they were not too tired at the end of the experiment. As expected, end-effectors performed significantly better when rendering virtual objects showing appropriate haptic characteristics, i.e., E1 was better at rendering objects featuring different edges and slanted surfaces, E2 at rendering objects featuring different curvature characteristics, and E3 at rendering objects featuring different stiffness characteristics. This result shows that is indeed important to tailor the end-effector to the interaction at hand, supporting the need for such modular haptic interfaces.

The weight of the device (160 g without end-effector) is one of its main limitations, that should be addressed in future work, as longer tasks might fatigue the users. Another limitation of the device is the range of motion of the articulated legs, that can only actuate the end-effector along 4-DoF. Future work should extend the range of possible motions, likely adding an additional articulated leg. Miniaturization of the device could enable the design of similar interfaces for the fingertips, significantly enlarging the range of applications in which the device can be used. Further optimizations in terms of mechanical structure, materials and manufacturing technologies will lead to better performance in terms of precision, repeatability, and applicable force. Moreover, personalization approaches such as [28], [29] can be used to achieve designs optimized for one's specific hand size, which can vary quite much across humans; similarly, task-driven techniques such as [30] can be used to design end-effectors optimized for certain types of interactions and environments. Finally, using DC motors instead of servos would enable a better control of the torque imparted, enabling a direct force control loop, which is often beneficial for haptic applications.

Appendix
Force Characterization for the Elastic Rubber End-Effector (E3)

As detailed in Sec. III-B.E3, the elastic rubber end-effector (E3) can be stretched by moving the two arms endpoints A and B farther from each other, enabling the device to control the stiffness of the end-effector surface. This Section analyzes and evaluates the relationship between the stretch δ applied to the end-effector, defined in eq. (19), and its stiffness. For the sake of simplicity, we consider a simplified elastic model for our end-effector, assuming a direct coupling

between the horizontal stretch of the elastic strip (axis x in Fig. 2) and its stiffness along the vertical direction (axis y). Of course, more complex models can be employed, so as to better characterize the stiffness coefficients of the strip along the different directions [31].

Fig. 9 presents the experimental setup we used for this identification procedure. A force sensor Nano43 (ATI Industrial Automation, US) is attached right below the upper body of the device, while a 3D-printed spherical shape is mounted between the sensor and the end-effector, mimicking the user's palm. We

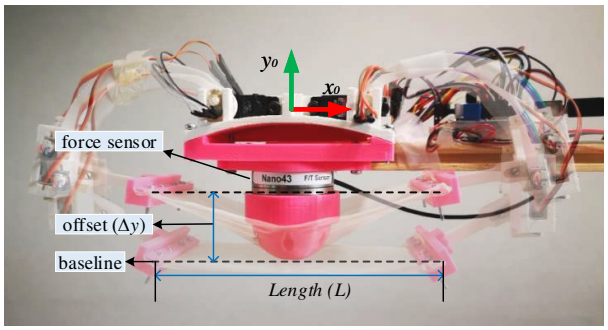

Fig. 9. Force characterization for the elastic rubber end-effector (E3): experimental setup. The force sensor is fixed right below the upper body of the device, while a 3D-printed spherical shape is mounted between the sensor and the end-effector. The figure shows two configurations of the device. In the first one, the end-effector barely touches the spherical shape (i.e., the baseline position); in the second one, the end-effector applies a force to the spherical shape and, in turn, to the sensor (i.e., its moves upwards of a certain offset Δy with respect to the baseline position). Increasing the distance L between A and B, i.e., horizontally stretching the end-effector, we can control its stiffness during the interaction.

model the interaction force f between the spherical shape and the end-effector as a linear function of the movement along the vertical axis, Δy (see Fig. 9):

$$f = k(\delta)\Delta y \tag{24}$$

where $k(\delta)$ represents the dependence of the stiffness coefficient k on the stretch δ of the elastic rubber end-effector, and Δy is the relative displacement along the vertical axis y between the current position of the end-effector and the rest/baseline position, i.e., when the end-effector is barely in contact with the spherical shape.

We consider a set of 18 stretches $\mathcal{D} = \{\delta_1, \ldots, \delta_i, \ldots, \delta_{18}\}$, satisfying eq. (18) and actuated following the control presented in Sec. III-C. For each stretch configuration $i = 1, \ldots, 18$, we moved the end-effector upwards, from its rest/baseline position until the maximum possible offset (see Fig. 9), and back. Throughout these movements, we registered the position of the end-effector and the corresponding forces applied to the force sensor along the vertical axis y. From the collected data, we can define the i-th estimated stiffness coefficient related to the end-effector stretch δ_i as

$$k_i = \hat{k}(\delta_i) = \mathbf{\Delta y}_i^{\#} \mathrm{f}_i, \tag{25}$$

where f_i and $\mathbf{\Delta y}_i$ denote the corresponding vectors of measurements acquired during the motion, and $(\cdot)^{\#}$ is the least-square pseudo-inverse operator. Finally, we use sets (δ_i, k_i) to fit a quadratic polynomial regression, i.e., a vector of

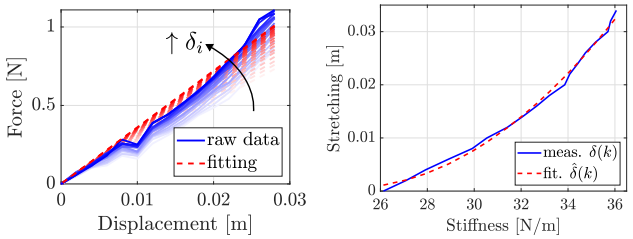

Fig. 10. Force characterization for the elastic rubber end-effector (E3): results. (a) Stiffness identification along the considered stretch configurations. Opacity of the plots increases as the stretch δ_i increases. (b) Results of the quadratic polynomial regression fit to estimate the function $\delta(k)$ relating the end-effector stiffness k along the normal direction with its stretch δ.

coefficients $(a, b, c)^T$ such that $\delta(k) = ak^2 + bk + c$, given the estimated stiffness coefficients k, best fits the measured stretch δ for the considered measurements.

Results of this stiffness identification across different stretch values of the end-effector are summarised in Fig. 10a. For each stretch δ_i, the force-displacement relationship is displayed, comparing the force $\hat{\mathrm{f}}_i = \hat{k}(\delta_i)\mathbf{\Delta y}_i$ resulting from eq. (25) (dashed red lines) with the force measured by the sensor (blue lines). Results show that the range of renderable stiffness is $[26, 36]$ N/m. Fig. 10b shows the quadratic polynomial regression fit, with the estimated coefficients being $(a, b, c)^T = (0.0002, -0.0120, 0.1478)^T$.

These results show that, to a certain extent, we can adjust the stiffness of the end-effector surface by stretching it. Sections III-B.E3 and III-C details how to control this parameter during the interaction with virtual or remote environments.

REFERENCES

[1] C. Pacchierotti, S. Sinclair, M. Solazzi, A. Frisoli, V. Hayward, and D. Prattichizzo, "Wearable haptic systems for the fingertip and the hand: taxonomy, review, and perspectives," *IEEE Trans. Haptics*, vol. 10, no. 4, pp. 580–600, 2017.

[2] D. Leonardis, M. Barsotti, C. Loconsole, M. Solazzi, M. Troncossi, C. Mazzotti, V. Parenti Castelli, C. Procopio, G. Lamola, C. Chisari *et al.*, "An EMG-controlled robotic hand exoskeleton for bilateral rehabilitation," *IEEE Trans. Haptics*, 2015.

[3] C. J. Nycz, T. Bützer, O. Lambercy, J. Arata, G. S. Fischer, and R. Gassert, "Design and characterization of a lightweight and fully portable remote actuation system for use with a hand exoskeleton," *IEEE Robotics and Automation Letters*, vol. 1, no. 2, pp. 976–983, 2016.

[4] R. M. Khurshid, N. Fitter, E. Fedalei, and K. Kuchenbecker, "Effects of grip-force, contact, and acceleration feedback on a teleoperated pick-and-place task," *IEEE Trans. Haptics*, May 2016.

[5] B. Lim, C. Lee, and D. Hwang, "Development of embedded sensor system for 5-dof finger-wearable tactile interface," *IEEE/ASME Trans. Mechatronics*, vol. 26, no. 4, pp. 1728–1736, 2021.

[6] I. Sarakoglou, N. G. Tsagarakis, and D. G. Caldwell, "A compact tactile display suitable for integration in VR and teleoperation," in *Proc. IEEE International Conference on Robotics and Automation (ICRA)*, 2012, pp. 1018–1024.

[7] M. Gabardi, M. Solazzi, D. Leonardis, and A. Frisoli, "A new wearable fingertip haptic interface for the rendering of virtual shapes and surface features," in *Proc. IEEE Haptics Symposium*, 2016, pp. 140–146.

[8] D. Trinitatova and D. Tsetserukou, "Touchvr: A wearable haptic interface for vr aimed at delivering multi-modal stimuli at the user's palm," in *Proc, SIGGRAPH Asia XR*, 2019, pp. 42–43.

[9] K. Minamizawa, S. Kamuro, N. Kawakami, and S. Tachi, "A palm-worn haptic display for bimanual operations in virtual environments," in *Proc. Intl. Conf. Human Haptic Sensing and Touch Enabled Computer Applications*, 2008, pp. 458–463.

[10] D. Trinitatova and D. Tsetserukou, "Deltatouch: a 3d haptic display for delivering multimodal tactile stimuli at the palm," in *2019 IEEE World Haptics Conference (WHC)*. IEEE, 2019, pp. 73–78.

[11] M. Altamirano Cabrera and D. Tsetserukou, "Linkglide: a wearable haptic display with inverted five-bar linkages for delivering multi-contact and multi-modal tactile stimuli," in *Proc. International AsiaHaptics Conference*, 2018, pp. 149–154.

[12] M. Dragusanu, A. Villani, D. Prattichizzo, and M. Malvezzi, "Design of a wearable haptic device for hand palm cutaneous feedback," *Frontiers in Robotics and AI*, p. 254, 2021.

[13] C. Pacchierotti, G. Salvietti, I. Hussain, L. Meli, and D. Prattichizzo, "The hRing: a wearable haptic device to avoid occlusions in hand tracking," in *Proc. IEEE Haptics Symposium*, 2016.

[14] A. Girard, M. Marchal, F. Gosselin, A. Chabrier, F. Louveau, and A. Lécuyer, "Haptip: Displaying haptic shear forces at the fingertips for multi-finger interaction in virtual environments," *Frontiers in ICT*, vol. 3, p. 6, 2016.

[15] F. Chinello, C. Pacchierotti, J. Bimbo, N. G. Tsagarakis, and D. Prattichizzo, "Design and evaluation of a wearable skin stretch device for haptic guidance," *IEEE Robotics and Automation Letters*, vol. 3, no. 1, pp. 524–531, 2017.

[16] M. A. Cabrera, J. Tirado, J. Heredia, and D. Tsetserukou, "Linkglide-s: A wearable multi-contact tactile display aimed at rendering object softness at the palm with impedance control in vr and telemanipulation," pp. 647–652, 2022.

[17] F. Chinello, C. Pacchierotti, M. Malvezzi, and D. Prattichizzo, "A three revolute-revolute-spherical wearable fingertip cutaneous device for stiffness rendering," *IEEE Trans. Haptics*, vol. 11, no. 1, pp. 39–50, 2017.

[18] Z. F. Quek, S. B. Schorr, I. Nisky, A. M. Okamura, and W. R. Provancher, "Sensory augmentation of stiffness using fingerpad skin stretch," in *Proc. IEEE World Haptics Conf.*, 2013, pp. 467–472.

[19] S. Pabon, E. Sotgiu, R. Leonardi, C. Brancolini, O. Portillo-Rodriguez, A. Frisoli, and M. Bergamasco, "A data-glove with vibro-tactile stimulators for virtual social interaction and rehabilitation," in *Proc. Annual Int. Workshop on Presence*, 2007.

[20] T. K. Moriyama, A. Nishi, R. Sakuragi, T. Nakamura, and H. Kajimoto, "Development of a wearable haptic device that presents haptics sensation of the finger pad to the forearm," in *Proc. IEEE Haptics Symposium (HAPTICS)*, 2018, pp. 180–185.

[21] C. Wee, K. M. Yap, and W. N. Lim, "Haptic interfaces for virtual reality: Challenges and research directions," *IEEE Access*, vol. 9, pp. 112 145–112 162, 2021.

[22] E. Bouzbib, M. Teyssier, T. Howard, C. Pacchierotti, and A. Lécuyer, "Palmex: Adding palmar force-feedback for 3d manipulation with haptic exoskeleton gloves," *IEEE Trans. Visualization and Computer Graphics*, 2023.

[23] E. Whitmire, H. Benko, C. Holz, E. Ofek, and M. Sinclair, "Haptic revolver: Touch, shear, texture, and shape rendering on a reconfigurable virtual reality controller," in *Proc. CHI conference on human factors in computing systems*, 2018, pp. 1–12.

[24] L. Kuang, M. Malvezzi, M. Ferro, D. Prattichizzo, P. Robuffo Giordano, F. Chinello, and C. Pacchierotti, "A 4-DoF Wearable Hand Device for Haptic Rendering of Surfaces and Edges," 2023, preprint. [Online]. Available: https://inria.hal.science/hal-04122137

[25] L. Kuang, F. Chinello, P. R. Giordano, M. Marchal, and C. Pacchierotti, "Haptic mushroom: a 3-dof shape-changing encounter-type haptic device with interchangeable end-effectors," in *Proc. IEEE World Haptics Conference (WHC)*, 2023.

[26] L. Sciavicco and B. Siciliano, *Modelling and control of robot manipulators*. Springer Science & Business Media, 2001.

[27] X. de Tinguy, C. Pacchierotti, M. Marchal, and A. Lecuyer, "Toward universal tangible objects: Optimizing haptic pinching sensations in 3d interaction," in *Proc. IEEE Conference on Virtual Reality and 3D User Interfaces (VR)*, 2019, pp. 321–330.

[28] M. Malvezzi, F. Chinello, D. Prattichizzo, and C. Pacchierotti, "Design of personalized wearable haptic interfaces to account for fingertip size and shape," *IEEE Trans. Haptics*, vol. 14, no. 2, pp. 266–272, 2021.

[29] E. M. Young, D. Gueorguiev, K. J. Kuchenbecker, and C. Pacchierotti, "Compensating for fingertip size to render tactile cues more accurately," *IEEE Transactions on Haptics*, vol. 13, no. 1, pp. 144–151, 2020.

[30] C. Pacchierotti, E. M. Young, and K. J. Kuchenbecker, "Task-driven pca-based design optimization of wearable cutaneous devices," *IEEE Robotics and Automation Letters*, vol. 3, no. 3, pp. 2214–2221, 2018.

[31] B. Woodward and M. Kashtalyan, "Three-dimensional elasticity solution for bending of transversely isotropic functionally graded plates," *European J. Mechanics-A/Solids*, vol. 30, no. 5, pp. 705–718, 2011.

Lisheng Kuang is a PhD candidate at CNRS-IRISA in Rennes, France. He got a master degree of control engineering from Harbin Institute of Technology (Shenzhen), in 2017. He was a research associate at the Italian Institute of Technology, Genova, Italy in 2019. He had five months visiting the Extended Reality and Robotics (xR²) Lab at Aarhus University in 2022. His research focuses on the design, prototyping, testing, and control of wearable robots for applications in human mobility aids.

Monica Malvezzi (M'12) is an Associate Professor at the University of Siena and Visiting Scientist at the Istituto Italiano di Tecnologia in Genova. She earned her Ph.D. degree in applied mechanics from the University of Bologna in 2003. She has also been Associate Professor of mechanics and mechanism theory at the University of Siena from 2008 to 2018, and Researcher at the University of Florence from 2002 to 2008. Her main research interests include control of mechanical and mechatronic systems, robotics, haptics, vehicle localization, multibody dynamics, grasping, and dexterous manipulation.

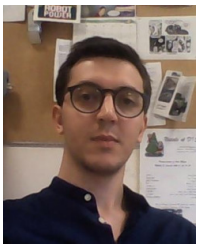

Marco Ferro is a postdoc at CNRS-IRISA in Rennes, France, since 2022. He was previously postdoc at the Department of Computer, Control, and Management Engineering (DIAG) of Sapienza University of Rome, Italy, where he got also his Ph.D. in Automation, Bioengineering and Operational Research, in 2019. He visited the LIRMM in Montpellier in 2014 as intern, and he was a visting Ph.D student at CNRS-IRISA in Rennes in 2018. Throughout his Ph.D. and the subsequent postdoc experience, he worked on vision-based control and estimation methods for humanoid and surgical robots, focusing later on scientific and technological problems in the medical robotics domain.

Paolo Robuffo Giordano (SM'16) received his MSc in Computer Science Engineering in 2001, and his PhD in Systems Engineering in 2008, both from the University of Rome "La Sapienza". In 2007 and 2008 he spent one year as a Postdoc at the Institute of Robotics and Mechatronics of the German Aerospace Center (DLR), and from 2008 to 2012 he was Senior Research Scientist at the Max Planck Institute for Biological Cybernetics in Tübingen, Germany. He is currently a senior CNRS researcher head of the Rainbow group at IRISA and Inria in Rennes, France. He received the 2018 IEEE Robotics and Automation Letters best paper award, and he is Editor of the IEEE Transactions on Robotics.

Francesco Chinello (M'19) got in 2014 his PhD degree on Information Engineering and Robotics, at the University of Siena (Italy). After his Post-Doc at the University of Siena and at the Italian Institute of Technology (Italy), he continued his career at the BTECH department, Aarhus University (Denmark) as a teacher and researcher, co-responsible of the Extended Reality and Robotics lab (XR^2). His research interests are in Haptics, Robotics applications and VR technologies.

Domenico Prattichizzo (F'15) is Full Professor of Robotics at the University of Siena, Senior Scientist at the Istituto Italiano di Tecnologia in Genova, and co-founder of WEART. He received the Ph.D. degree in robotics and automation from the University of Pisa in 1995. In 1994, he was a Visiting Scientist with the MIT AI Laboratory. He received the IEEE 2009 Chapter of the Year Award. He served as the Vice-Chair for Special Issues of the IEEE Technical Committee on Haptics and the Chair of the Italian Chapter from the IEEE RAS, from 2006 to 2010. He also served as the Chair for the IEEE RAS Early Career Awards Evaluation Panel in 2013. He serves as the Editor-in-Chief for the IEEE Transactions on Haptics. He is the author of more than 200 articles on the topics of haptics, grasping, visual servoing, mobile robotics, and geometric control.

Claudio Pacchierotti (SM'20) is a tenured researcher at CNRS-IRISA in Rennes, France, since 2016. He was previously a postdoctoral researcher at the Italian Institute of Technology, Genova, Italy. Pacchierotti earned his PhD at the University of Siena in 2014. He was Visiting Researcher in the Penn Haptics Group at University of Pennsylvania in 2014, the Dept. of Innovation in Mechanics and Management at University of Padua in 2013, the Institute for Biomedical Technology and Technical Medicine (MIRA) at University of Twente in 2014, and the Dept. Computer, Control and Management Engineering of the Sapienza University of Rome in 2022. Pacchierotti received the 2014 EuroHaptics Best PhD Thesis Award and the 2022 CNRS Bronze Medal. He is Senior Chair of the IEEE Technical Committee on Haptics, Co-Chair of the IEEE Technical Committee on Telerobotics, and Secretary of the Eurohaptics Society.